



Electron-withdraw groups functionalized MOFs for efficient nitric oxide enrichment and simultaneous removal

Jingjing Zhao ¹, Shuangjun Li ¹, Rui Liang, Qing Wang, Yi Li, Xiaoyan Liu ^{*}, Dieqing Zhang ^{*}, Hexing Li ^{*}

The Education Ministry Key Lab of Resource Chemistry, Joint International Research Laboratory of Resource Chemistry, Shanghai Key Laboratory of Rare Earth Functional Materials, Shanghai Frontiers Science Center of Biomimetic Catalysis, College of Chemistry and Materials Science, Shanghai Normal University, Shanghai 200234, China



ARTICLE INFO

Keywords:
 NO_x oxidation
 Photocatalysis
 MOFs
 -NO₂ functionalization
 Synergistic effect

ABSTRACT

Nitric oxide (NO) is one of the major pollutants in the air and the removal of dilute NO still faces challenges of low efficiency. Herein, an electron-withdraw groups functionalized metal-organic frameworks (MOFs) was reported as photocatalyst for the efficient removal of NO. The UiO-66 was conferred with nitro groups (-NO₂), showing narrow band gap due to the conjugate with the electron cloud on the benzene ring, leading to deep color of this photocatalyst and high visible light sensitivity. Meanwhile, the electron acceptor -NO₂ greatly increased the adsorption toward electron donor NO molecules. Resultingly, a high NO (550 ppb) removal rate of 83% and 76% were achieved under visible-light irradiation ($\lambda > 400$ nm) under dry and moist condition, respectively. This work provides a new strategy for the regulation of MOFs based photocatalysts, which may be applied in the treatment of air pollutants such as NO removal.

1. Introduction

The large amount of NO_x (NO 90%) produced by human activities is one of the major air pollutants, which can destroy the ozone layer, produce photochemical smog and cause many premature deaths of life [1,2]. With awareness of environmental protection[3], it is urgent to develop a method for effective nitrogen oxides removal. To this end, many methods including selective noncatalytic reduction (SCR/SNCR) technologies[4–6], physical adsorption[7], electrochemical process[8] and photocatalysis technology[9] have been studied. SCR technology has been recognized as the most effective one to remove more than 90% of NO_x pollutants, which is widely used in various tail gas treatments. However, it requires expensive noble metal catalysts and consumes energy while being powerless against the low concentration of NO_x (ppb-level) in the atmosphere[10,11]. The wide temporal and spatial distribution, large fluctuations, and uncontrollable atmospheric reaction media and conditions make the removal of low-concentration gas pollutants in the atmosphere a great challenge.

Photocatalysis, an effective technology driven by sunlight, which is not limited by time and space due to the environmentally friendliness

and mild reaction conditions, has shown great potential in removing low concentration NO gas. In general, oxidation of NO to nitrate is one of the most reasonable ways at present. Most of the related researches focused on the ultraviolet region[12,13], which only accounts for 5% of the total sunlight, and the utilization rate of light energy is low. Therefore, the development of visible-light catalysts has positive practical significance.

Metal-organic frameworks (MOFs), a class of crystalline porous materials composed of metal ions/clusters and organic linkers, has been widely used in gas storage and absorption, chemical sensors, electro-catalysis and photocatalysis. Compared with traditional catalysts, it has unique advantages such as large surface, intrinsically porous structure and controllable functional groups[14,15]. However, most MOFs such as ZIF-8[16], UiO-66[17], MIL-125[18,19], etc. have a relatively large energy band gap, because the coordination groups (-COOH in most cases) usually possess a small π -orbital conjugation[20]. However, this wide band gap severely limits the utilization of long wavelength light, leading to low photocatalytic efficiency. The modification of MOFs with functional groups on the ligands is a promising strategy. It can enhance the adsorption capacity, increase the specific surface area and porosity or improve the light absorption capacity of MOFs. Notably, -NH₂ is the

^{*} Corresponding authors.

E-mail addresses: xyliu@shnu.edu.cn (X. Liu), dqzhang@shnu.edu.cn (D. Zhang), hexing-li@shnu.edu.cn (H. Li).

¹ These authors contributed equally to this work.

most widely used functional group to improve the light absorption ability of MOFs, such as NH₂-UiO-66[21], and NH₂-MIL-125[22]. Other substituent groups, including nitro-group(-NO₂), the methylthio group (-SCH₃)[23], -Br and -OH also have been explored to tune the structure of MOFs for effective visible light adsorption[24]. Among which, the -NO₂, with electron absorbing properties, has attracted some attention recently[25–27]. It is a chromophore that can improve the light absorption ability of the MOFs through electron cloud conjugation, which may improve the photocatalytic efficiency of NO oxidation due to the expanded light adsorption. Moreover, the enrichment of NO reductant on the surface of photocatalyst is another key factor for high NO oxidation efficiency. NO is a kind of electron-rich molecules containing 2-electron π bond and a 3-electron π bond. Fortunately, the electrophilic-NO₂ group has great potential in promoting adsorption towards NO molecules, which may highly improve the photocatalytic efficiency. Taking all the above in consideration, the study of photocatalytic oxidation of NO on -NO₂ modified MOFs is highly desirable.

Herein, the -NO₂-modified UiO-66(Zr) was prepared by the microwave-assisted solvent-thermal method for efficient visible-light-driven photocatalytic removal of NO. The functional -NO₂ groups was successfully coordinated with UiO-66(Zr) via pre-functionalization strategy. The modification of -NO₂ group not only lowered the band gap from 3.91 eV to about 2.71 eV and greatly enhanced the visible-light adsorption capability of UiO-66(Zr), but also increased the adsorption of NO gas and O₂ significantly. Resultingly, the conversion rate of NO could reach 76% in humid and 83% in dried atmosphere, respectively. A very low concentration of NO₂ byproduct gas was detected. The modification of electrophilic -NO₂ groups onto MOFs is proved to be an effective strategy for enhanced light utilization and the enrichment of NO, which may pave a new avenue for the photocatalytic removal of gas phase pollutants by MOFs based photocatalysts.

2. Experimental section

2.1. Materials

Zirconium tetrachloride (ZrCl₄), terephthalic acid (H₂BDC), ethanol (EtOH), potassium iodide (KI), p-quinone (PBQ, 99%), tert-butyl alcohol (TBA), potassium dichromate(K₂Cr₂O₇) and N/N-dimethylformamide (DMF) were purchased from Aladdin, 2-nitroterephthalic acid (NO₂-H₂BDC) was obtained from Macklin. Hydrochloric acid (HCl) was obtained from Sinopharm Chemical Reagent Co., Ltd. (Shanghai, China). All the reagents were ACS Reagent grade and used without further purification.

2.2. Preparation of -NO₂ modified UiO-66(Zr) (NU) catalysts

The samples were prepared by a simple microwave solvothermal assisted method. Typically, 20 mL DMF and 932 mg ZrCl₄ was added to a clean quartz microwave reaction tube. After 5 min of ultrasonic dissolution, 845 mg of NO₂-H₂BDC and 0.67 mL HCl were added in sequence and stirring for 5 min. Subsequently, the mixture was treated under microwave irradiation in a microwave digestion system (Ethos TC. Milestone) at 120°C for 45 min with a heating rate of 10 °C/min. After the system cooled down to room temperature by circulating condensation system, the yellow power was separated by centrifugation with EtOH and DMF each for 4 times alternately. The as-prepared power was dried at 60°C for 12 h in a vacuum drying oven, which was named as NU-100. Then 25%, 50% and 75% of NO₂-H₂BDC were replaced with H₂BDC respectively to obtain UiO-66 modified with different amount of -NO₂ groups and named as NU-75, NU-50 and NU-25 respectively.

UiO-66(Zr) was synthesized by the same method except for replacing all the NO₂-H₂BDC with H₂BDC and named as NU-0.

2.3. Characterization

The basic morphologies of all the catalysts were determined by field emission scanning electron microscopy (FESEM, HITACHI S-4800) and transmission electronic micrograph (TEM, JEOL JEM-2010 F, 200 KV). The crystal structural characteristics were determined through the X-ray diffractometer (XRD, Rigaku DMax-3 C Cu K α radiation). The UV-vis diffuse reflectance spectra (DRS) were collected using a UV-vis spectrophotometer (DRS, Shimadzu UV-2450) to study the optical properties. To analyze electronic states, X-ray photoelectron spectroscopy (XPS) was measured on a PerkinElmer PHI 5000 C ESCA system and all the binding energies were calibrated by using the contaminant carbon (C1s = 284.8 eV) as the standard. The N₂ adsorption-desorption isotherms were measured via a Micromeritics ASAP 2010 instrument at 77 K and the specific surface area (S_{BET}) was calculated by applying Brunauer-Emmett-Teller (BET) models on desorption branches. Temperature-programmed desorption of O₂ (O₂-TPD) and NO (NO-TPD) were performed in Micromeritics Auto Chem II 2920. The Fourier transformation infrared spectrum (FTIR) were obtained on an AVATAR 370 FT-IR spectrometer. *In situ* diffuse reflectance infrared Fourier transform spectroscopy (*in situ* DRIFTS) (Nicolet iS50, Thermo Fisher Scientific) was used for *in situ* monitoring the possible surface intermediates over the catalysts within the *in situ* catalytic NO oxidation process. Electron paramagnetic resonance (EPR) spectroscopy measurement was carried out on a Bruker ESP A300 spectrometer, using 5, 5-dimethyl-1-pyrroline-N-oxide (DMPO) as trapping agent to monitor superoxide and hydroxyl radicals. The photoelectron-hole recombination was carried out on a fluorometer (PL, Cony Eclipse, Varian, USA). And the time-resolved PL spectra was analyzed by FLS1000 fluorescence spectrophotometer (Edinburgh Instruments).

According to the UV-vis diagram, the corresponding band gap energy is calculated by the Kubelka-Munk equation:

$$\alpha h\nu = A(h\nu - E_g)^n$$

where A, E_g, v, h and α represent the constant, band gap, optical frequency, Planck constant and absorption coefficient, respectively. n is equal to 1/2 or 2 corresponding to the indirect band gap or direct band gap of semiconductor.

2.4. Photocatalytic activity test

The photocatalytic activity of the as-formed photocatalyst was measured through photocatalytic NO removal tests in a continuous flow reactor (10.8 L) at ambient temperature. A xenon lamp (PLSSXE300, Perfect Light, China) with UV cut-off filter ($\lambda > 400$ nm) placed vertically above the reactor was served as a visible-light source. In the experiment system, 0.2 g of the catalyst was evenly dispersed and coated in two 12 cm diameter glass dishes through the ethanol, then dried in an oven of 80°C to obtain a catalyst film. The catalyst was sealed in the reaction chamber with an N₂ stream containing 550 ppb NO at the rate of 4.0 L/min (humidity level 75% or desiccative). After the NO and O₂ in the reactor reached adsorption-desorption equilibrium, the lamp was turned on immediately to trigger the photocatalytic reactions. An online chemiluminescence NO analyzer (Thermo Environmental Instruments Inc. Model 42i) was equipped to monitor the concentration of NO, NO₂ and NO_x constantly. The photograph and schematic illustration of the reaction system are shown in Fig. S1. Ultimately, the removal ratio of NO was calculated via the following equation:

$$\eta(\%) = \frac{C_0 - C}{C_0} * 100\%$$

Where η refers to the NO removal rate, C₀ refers to the concentration of NO after the adsorption-desorption equilibrium, and C is the real-time NO concentration detected after turning on the lamp.

2.5. Photoelectrochemical measurement

All the photoelectrochemical (PEC) tests were measured with a typical three-electrode process in 0.5 M Na₂SO₄ aqueous electrolyte via a CHI 760E electrochemical workstation. The samples with an active area of approximately 1.0 cm² on FTO glass served as the working electrode. Platinum plate and saturated calomel electrode (SCE) were used as counter electrode and the reference electrode, respectively. The conduction band position of the sample can be obtained according to the Mott-Schottky curves measured at different frequencies, and then the valence band position can be calculated by combining the band gap obtained by solid ultraviolet. The incident photon current efficiency (IPCE) of the samples were analyzed using the Zahner electrochemical workstation in the illumination range of 380–1020 nm.

2.6. Computational details

All theoretical calculations were completed based on the density functional theory (DFT) method as implemented in the Vienna ab initio simulation package (VASP). The frozen-core all-electron projector-augment-wave (PAW) was employed to study the interaction between ions and electrons. The exchange-correlation effect was investigated through the standard generalized gradient approximation (GGA) under Perdew-Burke-Ernzerhof (PBE) scheme. The energy cut-off for the plane-wave basis was set at 550 eV. The Brillouin zone integration was carried out on the Monkhorst-Pack k-points grids with resolution of 0.2 Å⁻¹. The dipole corrections were also introduced to minimize interaction between periodic images. The Grimme DFT-D3 dispersion correction with the Becke-Jonson damping was adopted to explain the weak van der Waals (VDW) interactions. During structural relaxation, the criteria for the force and energy difference were set to 0.005 eV/Å and 1.0 × 10⁻⁶ eV, respectively.

3. Results and discussion

3.1. Physical and chemical properties characterizations

The modified NO₂-UiO-66(Zr) were synthesized via microwave-assisted solvothermal method (Fig. 1a), during which the -NO₂

containing ligands were applied for the *in situ* modification. The schematic diagram of -NO₂ group connected to the UiO-66(Zr) is shown in Fig. S2. The FTIR were carried out to prove the existence of -NO₂ groups in NU-100. As shown in Fig. S3, the peaks at 1540 cm⁻¹ and 1305 cm⁻¹ can be clearly observed indexed to the asymmetric vibration of -NO₂ groups, indicating that was successfully coordinated to the NU-100 sample[28]. The optical images of NU samples also confirmed this result. As shown in Fig. 1b, NU samples have obvious color change from white to yellow gradually, along with the increased feed contents of containing ligands from 0% to 100%, which can be attributed to the increased -NO₂ groups in the samples (Fig. 1b). The X-ray diffraction (XRD) patterns of all the NU catalysts are shown as Fig. 1c. The NU-0 exhibited good crystalline structure with sharp and strong diffraction peaks which consist good with the typical peaks reported in the previous literature[29]. No obvious difference of the samples was observed, demonstrating that the modification of -NO₂ group has little influence on the crystallinity and structural integrity of NU catalysts. The field-emission scanning electronic microscopy (FESEM) images (Fig. S4a~e) demonstrated that the morphologies of NU samples were maintained well with the modification of -NO₂. The energy-dispersive X-ray spectroscopy (EDX) mappings of NU-100 (Fig. S4f~j) confirmed the existence and homogeneously distribution of Zr, C, O and N elements. The elemental bonding configurations were further studied through X-ray photoelectron spectroscopy (XPS) measurements (Fig. S5). The N1s spectra of NU-100 clearly show the oxidized N peak [30], indicating the presence of functional groups containing N, further support the successful introduction of -NO₂.

The specific surface area and pore structure of the samples were confirmed by adsorption-desorption isotherms, as shown in Fig. 1d and Table S1. Derived from N₂ sorption isotherms, the calculated Brunauer-Emmett-Teller (BET) surface area for NU-0 is 687 m²/g. With the introduction of -NO₂, the specific surface area of the samples decreased gradually due to the successfully coordinated -NO₂ groups[31–33]. For further information about the adsorption ability of NU samples towards NO molecules, NO temperature-programmed desorption (TPD) was carried out.

As shown in Fig. 1e, both NU-0, NU-100 show the wide peak of NO adsorption. Obviously, NU-0 showed good NO adsorption capacity both in the range of physical adsorption (100–250°C) and chemical

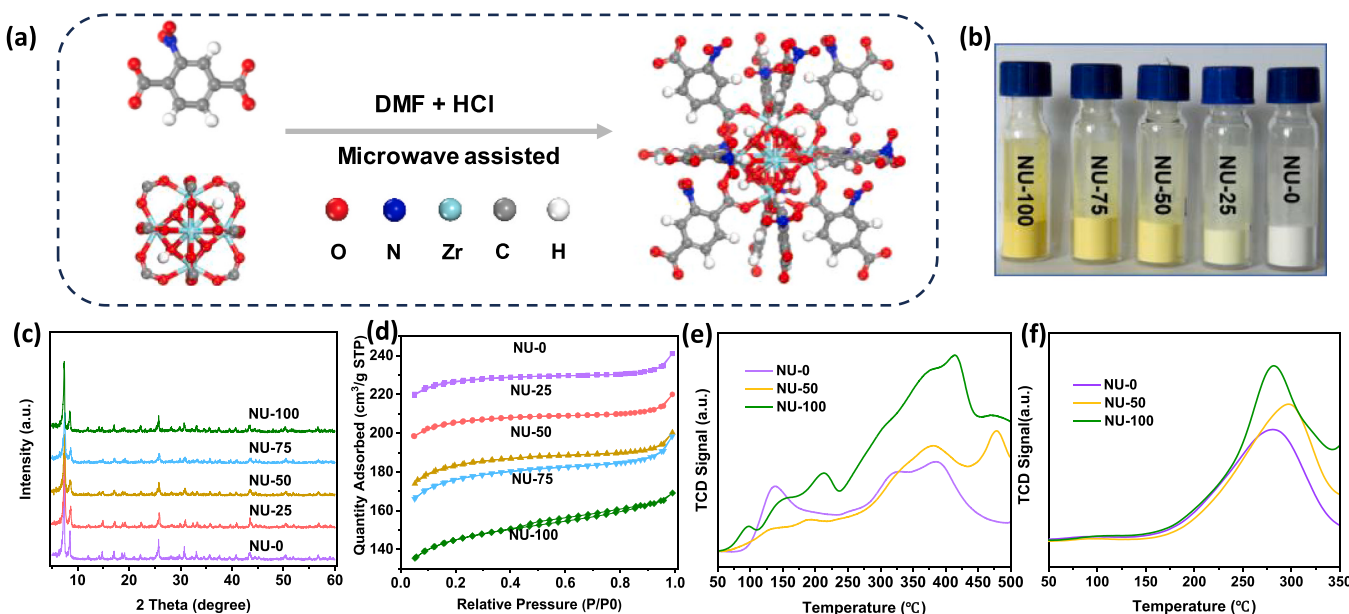


Fig. 1. (a) Schematic illustration of the synthesis process of NO₂-UiO-66(Zr). (b) The optical images of NU-samples with different content of -NO₂ coordinated ligands. (c) XRD patterns of the as-prepared samples. (d) Nitrogen adsorption-desorption isotherms of different samples. (e) NO-TPD profiles and (f) O₂-TPD profiles of NU-0, NU-50 and NU-100.

adsorption (300–500°C). Notably, after the introduction of -NO_2 groups, the adsorption area of the sample for NO increased significantly, and the adsorption temperature shifted to the higher region, indicating that the enhanced adsorption of NO. NU-100 showed a larger adsorption area and a higher adsorption temperature. It is worth pointing out that NU-100 shows the minimum specific surface area of $445 \text{ m}^2/\text{g}$, however, the strongest NO adsorption. This result confirmed the ability of enrichment of NO molecules of NU-100. As another reductant, O_2 -TPD was also measured. It is clear that NU-100 also has promoted adsorption towards O_2 according to the enlarged adsorption area (Fig. 1f). Generally, the adsorbed oxygen species change in the following sequence: O_2 (ad) \rightarrow O_2 (ad) \rightarrow O^- (ad) \rightarrow O_2^- (latt)[34–36]. The peak around 100°C can be assigned to physically adsorbed oxygen. Additionally, NU-0 and NU-100 displayed remarkable O_2 desorption peaks in the range from 150 to 350°C, which usually be assigned to the desorption of adsorbed oxygen species (O_2^- (ad) and O^- (ad)). The broader desorption peak in the high-temperature region and the higher adsorption area of NU-100 suggesting the stronger oxygen binding capability compared to NU-0, which was favorable for achieving an efficient oxygen-activated photocatalytic NO oxidation [37,38].

In order to further study the light adsorption ability of NU samples, UV-vis diffuse reflectance spectra (DRS) were carried out. As shown in Fig. 2a, NU-0 showed absorption band below 320 nm with no significant absorption peaks in the visible region, while, after modified with -NO_2 groups, the sample NU-100 showed extended light adsorption to the visible light region from 320 nm to 500 nm. With the increasing amount of -NO_2 groups, the NU samples show extended absorption in the visible region gradually. NU-100 exhibited the best absorption properties of visible light, attributing to the functional -NO_2 groups, which is a chromophore group and also an electron-absorbing group[39]. When -NO_2 groups modified on terephthalic acid, they will form conjugation with benzene ring to increase the delocalization degree of electron cloud. The more such conjugated components are, the darker the color of the catalyst will be, and meanwhile, it becomes more conducive to the absorption of visible light. The above results are consistent with the color change trend of the catalyst in Fig. 1b.

Kubelka-Munk formula (based on the equation $(Ahv)^2 = a(hv - Eg)$) is used to calculate the band gap of different samples. As shown in Fig. 2b, the band gap of NU-0 without -NO_2 groups modification is 3.91 eV, which is a typical photocatalyst driven by ultraviolet. However, with the introduction of -NO_2 groups, the band gaps decrease gradually. As

shown in Table S2, the band gap of NU-100 is 2.71 eV, which is much narrower than that of NU-0, demonstrating that it was successfully changed into a visible-light-driven catalyst. To further explore the exact valence band (VB) and conduction band (CB) of all the samples, Mott-Schottky electrochemical measurements in different frequencies were carried out to gain the detailed information about the energy-level alignment. The positive slopes of the Mott-Schottky plots were achieved, suggestive of a n-type semiconductor behavior. The intersection of the tangents of the Mott-Schottky curve at different frequencies is the flat band potential of the material. Fig. S6 depicted the Mott-Schottky curves of samples NU-25, NU-50, NU-75, and NU-100 at frequencies from 500 Hz to 1500 Hz, showing the flat band potentials (E_{FB}) of -0.67 , -0.57 , -0.55 and -0.59 eV, respectively. The CB and VB position of the material can be obtained by the flat band potential and E_g . The detailed positions of the VB and CB of the catalysts are shown in Table S2 and Fig. 2c. The modified -NO_2 groups on $\text{UiO-66}(\text{Zr})$ effectively change the CB position, while slightly affect the position of the VB. Due to the intrinsic electron-withdraw character of the -NO_2 groups, the VB orbital energy increased, resulting in the reduced bandgaps and more conducive to absorb visible light. This is consistent with the conclusions in the literature. The band gap of UiO-66 material remains basically unchanged, but after functionalization of -NO_2 , the π orbital of the benzene ring splits into two bands. One of the bands remains in place, while the other band containing functional group contributions moves upward, producing a fully filled gap state and a reduced effective band gap. Therefore, it is much easier to excite connected electrons from this newly split gap state. So the narrowed band gap is achieved with -NO_2 functionalization [40]. Since the redox potential of NO to NO_3^- is 0.96 eV [41], the photogenerated holes of the NU samples can oxidize NO to NO_3^- directly.

The photoelectrochemical performance was evaluated. Incident photon-electron conversion efficiency (IPCE) measurements were carried out to study the light utilization (Fig. 2d). The increasing photoelectric conversion efficiency of NU-50 and NU-100 than NU-0 indicated that the NU samples possess super visible light response and excellent separation efficiency of photo-generated electrons and holes, which are consistent with the result of UV-vis spectra above. From the chronoamperometric I-t curves in Fig. 2e, with the increase of -NO_2 groups content, the as-formed samples showed increased photocurrent density of visible-light, which means the modification of -NO_2 groups improved the generation of photo electrons and the separation rate of these photo-

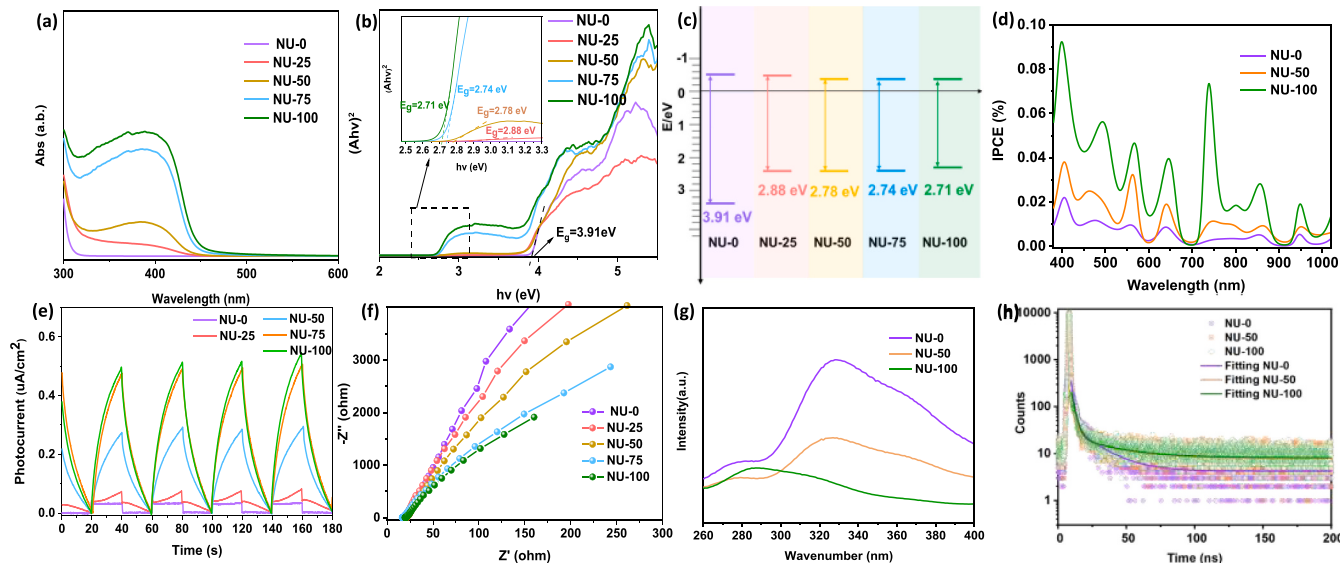


Fig. 2. (a) UV-vis diffuse reflectance spectra of NU-samples. (b) Calculated band gap energies of different samples by Kubelka-Munk transformation, (c) band gaps and band positions of different NU samples. (d) IPCE measurements, (e) photocurrent responses, (f) electrochemical impedance spectra (EIS) of NU samples under visible light irradiation ($\lambda > 400 \text{ nm}$). (g) The steady-state PL spectra and (h) Corresponding time-resolved PL spectra.

generated electrons and holes. The electrochemical impedance data (EIS) further confirmed the result. NU-100 showed the smallest arc radius of all the samples, showing lower electronic resistance (Fig. 2f). The weaker room-temperature steady-state photoluminescence (PL) spectra peak of NU-100 (Fig. 2g) demonstrated a low recombination rate of photo-generated electrons and holes, which could further confirm the higher photocurrent. Furthermore, according to the time-resolved PL spectroscopy (Fig. 2h and Table S4), the average emission lifetime of NU-100 was 15.65 ns, much longer than that of NU-0 (9.85 ns), indicating the longer lifetimes of charge carriers[42,43].

As a photocatalyst, strong and broad light absorptions is the fundamental criterion, is an important factor for efficient photocatalysis[44]. To further understanding the light adsorption properties of the above NU-samples, theoretical calculations were performed. The configuration models of NU-0, NU-50 and NU-100 samples are as displayed in Fig. 3a-c, subsequent calculations will be based on this model. The effect of -NO₂ modification on the band structure of NU catalysts was investigated by calculating the density of states (DOS). The partial density of states (PDOS) plots is as presented in Fig. S7. According to the total density of states (TDOS), as displayed in Fig. 3d, the calculated absorption edges are 2.41, 2.24, 2.18 eV for NU-0, NU-50, and NU-100 respectively, corresponding to the respective band gap values[45]. Clearly, an increase of -NO₂ groups content in NU leads to the negative shift to lower energy of the absorption edges coefficient, agreeing well with the results of UV-vis (Fig. 2a). The calculated values of absorption coefficient are presented in Fig. 3e. NU-100 and NU-50 after -NO₂ groups modification own a broader absorption spectrum from ultraviolet light to visible light compared to NU-0, further confirming that the introducing of -NO₂ modification could be beneficial for optical absorptions.

3.2. Photocatalytic activity and oxidation pathway of NO

The NO oxidation in a flowing gas phase reactor was performed under visible-light ($\lambda > 400$ nm) irradiation in dried condition to

evaluate the photocatalytic performances. As shown in Fig. 4a, NO cannot be oxidized in the presence of pure NU-0. Because NU-0 showed no visible light absorption capacity, which is consistent with the previous UV-vis results in Fig. 2a. However, the NO removal rate was significantly promoted upon conferring MOFs with -NO₂ groups. With the increased -NO₂ groups contents, NU samples exhibited promoted NO removal rate gradually. The NU-100 exhibited maximal photocatalytic activity with a removal rate up to 83%. The activity is better than that of most previously reported catalysts in similar systems (Table S5). To avoid the contribution of raw material, the NO removal test of NO₂-H₂BDC was performed under the same conditions and almost no removal is achieved (Fig. S8). Besides, the content of toxic by-product NO₂ was controlled at a low level under 20 ppb (Fig. 4b). In order to evaluate the photocatalytic stability of the as-prepared samples, the NU-100 was subjected to a continuous photocatalytic test up to 7 hours (Fig. 4c). It was surprising that a removal rate of 70% was still maintained and no accumulation of by-product of NO₂ was observed (Fig. S9). This may be attributed to the modified -NO₂ on the metal organic skeleton, which can selectively adsorb NO molecules due to the electron-absorbing property, favoring to the gathering of low concentration of NO gas on the catalyst surface. Besides, the large specific surface area of the NU-100 is conducive to providing more active centers and improving the stability of the catalyst. The SEM, XRD and FTIR characterization of the catalyst after the reaction show that there is no significant change in the morphology and structure of the catalyst before and after the reaction (Fig. S10-S12). Such excellent activity and stability indicated that the NU-100 could be served as a reliable photocatalyst for breaking down low concentration of NO from gas mixtures under flow conditions.

Generally, photogenic electron (e⁻), photogenic holes (h⁺), superoxide radical (-O₂[·]) and hydroxyl radical (-OH) are generated in photocatalytic reactions, which are important factors for the catalytic activity [46,47]. To further distinguish the active species and understand the mechanism, active species trap and control experiments were carried out by using various trapping agents. K₂Cr₂O₇, KI, p-benzoquinone

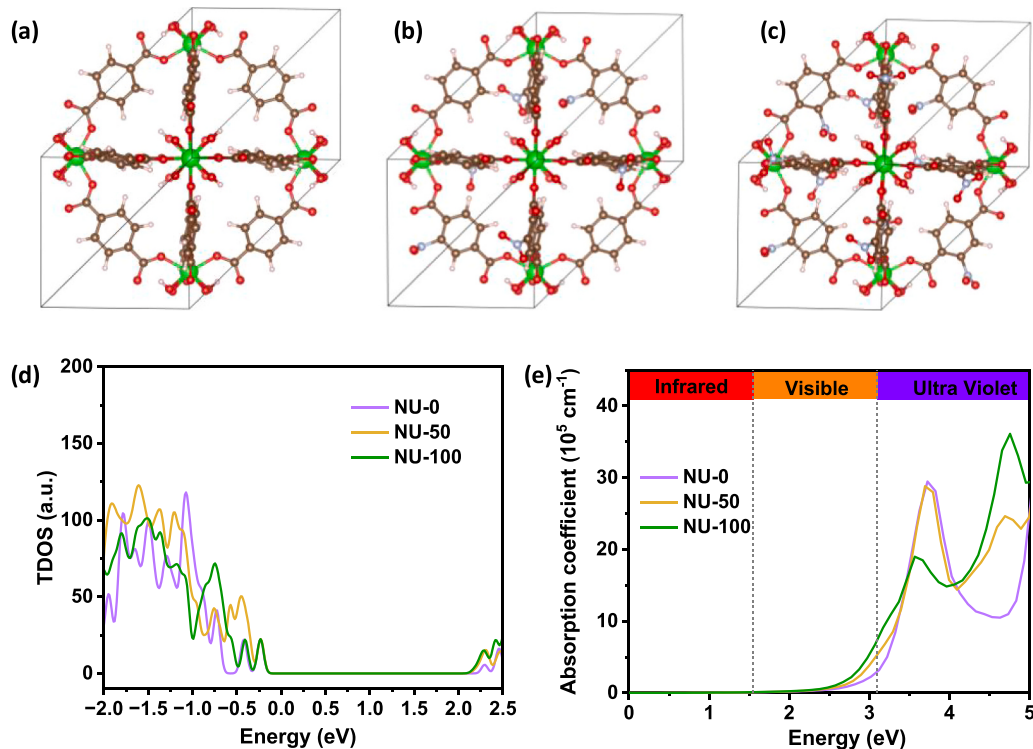


Fig. 3. DFT computational configuration of (a) NU-0, (b) NU-50, (c) NU-100 samples. (d) TDOS plots for NU-0, NU-50 and NU-100 samples. (e) Optical absorption coefficients of NU-0, NU-50 and NU-100 samples.

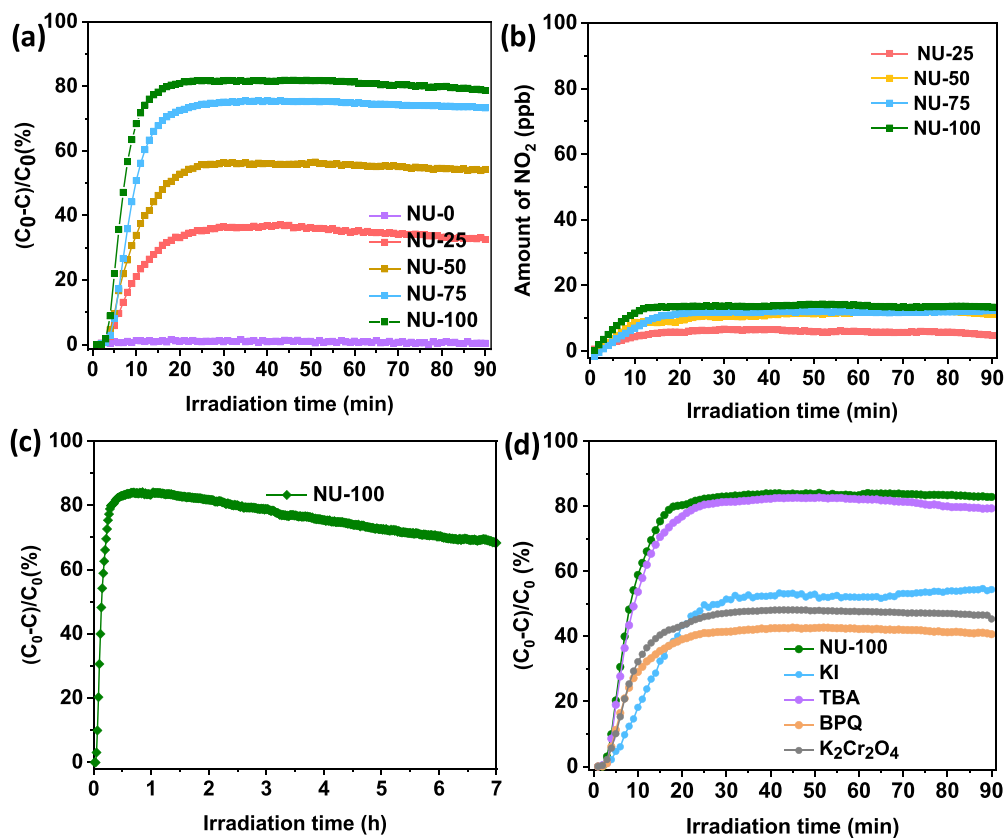


Fig. 4. (a) Photocatalytic NO removal rate over NU samples under dry atmosphere. (b) The corresponding amounts of by-product NO₂. (c) The durability test for photocatalytic NO oxidation over NU-100. (d) The photocatalytic performance of NO oxidation over NU-100 by using various trapping agents to capture active species.

(PBQ), and tert-butyl alcohol (TBA) were used to capture e^- , h^+ , $\cdot O_2$ and $\cdot OH$, respectively. As displayed in Fig. 4d, with trapping photo-generated h^+ and $\cdot O_2$ by KI and BPQ, the NO removal rate was decreased obviously, indicating that both h^+ and $\cdot O_2$ are the main active species in this reaction. In addition, the photocatalytic activity after trapping e^- with $K_2Cr_2O_4$ was decreased to 40%, and it almost coincided with the oxidation activity curve after capturing $\cdot O_2$ by BPQ. So, it is reasonable to conclude that $\cdot O_2$ may be derived from the reduction of oxygen by photo-generated electrons, and almost all the photoelectrons are captured by O_2 to generate $\cdot O_2$. While the activity barely changed before and after the addition of TBA as hydroxyl radical trapping agent because there may be no hydroxyl radical generation without water.

In practical atmospheric environment, NO is often existed accompanied by amount of water vapor. Therefore, our NO removal test was simulated under humid conditions with a humidifier. As shown in the Fig. 5a, all the NU samples with $\cdot NO_2$ groups modified have enhanced NO removal ability. NU-100 showed an outstanding NO removal effect under moist condition with additional water supply, reaching 76% removal rate at 90 minutes. Similarly, the NO₂ content in the reaction process was measured, and no extra NO₂ production and accumulation were detected (Fig. S13). The stability test shows that the catalyst can still maintain about 70% removal rate after 7 hours of long operation with little NO₂ production (Fig. 5b and Fig. S14), which provides a possible reference for the removal of low concentration of NO in the practical conditions. Obviously, NU-100 exhibits a faster response speed to NO removal in dried conditions (Fig. 5c). The corresponding first-order rate constants of NU-100 under dried condition was 0.183 min^{-1} , about 4.3 times higher than NU-100 under moist condition (0.043 min^{-1}) (inset Fig. 5c). The faster response speed showing superior performance than under moist conditions.

In the free radical trapping experiment, h^+ and $\cdot OH$ were also proved

to be the main active species in the system under moist condition (Fig. 5d). The difference is that after trapping $\cdot OH$ by TBA, the NO removal rate slightly decreased to 68%, suggesting that hydroxyl radicals also one of the active species in the oxidation of NO under such moist condition. That can be conclude that a small part of h^+ oxidizes H_2O to $\cdot OH$ in the photocatalytic process, and most of the h^+ participates in oxidizing NO directly. To sum up, the active species are mainly h^+ , $\cdot O_2$ and $\cdot OH$. This may account for the faster response speed of NU-100 under dried conditions. Under wet condition, the photogenic holes are firstly involved in oxidizing H_2O to $\cdot OH$ and then the $\cdot OH$ works as active species for NO oxidation under wet condition. This two-step process is slow. While, the photogenic holes can directly oxidize NO instead of the two-step oxidation process without the participation of supernumerary water. Thus, a faster NO removal rate was achieved under dry condition.

To further confirm the existence of reactive oxygen species (ROS) in NU-100, EPR paramagnetic-trapping experiments were carried out using 5, 5-dimethyl-1-pyrroline-N-oxide. After illuminating for 10 min, NU-100 shows remarkably intense hydroxyl radical peaks and superoxide radical peaks (Figs. 5e and 5f), confirming the existence of $\cdot O_2$ and $\cdot OH$ and they can serve as the ROS for the selective oxidation of NO.

3.3. Mechanism investigation

To further study the mechanism, *in situ* DRIFTS was performed to detect the intermediates and products under photocatalytic NO oxidation process with a continuous real-time monitoring (Fig. S15). Firstly, the spectrum of high purity air without NO under room temperature and dark condition was recorded as the background. Then, when NO gas was introduced to the reaction chamber, the NO absorption was detected. As shown in Fig. 6a, the peaks at 1063 cm^{-1} and 1274 cm^{-1} could be assigned to NO and N_2O_2 respectively, indicating the adsorption of NO

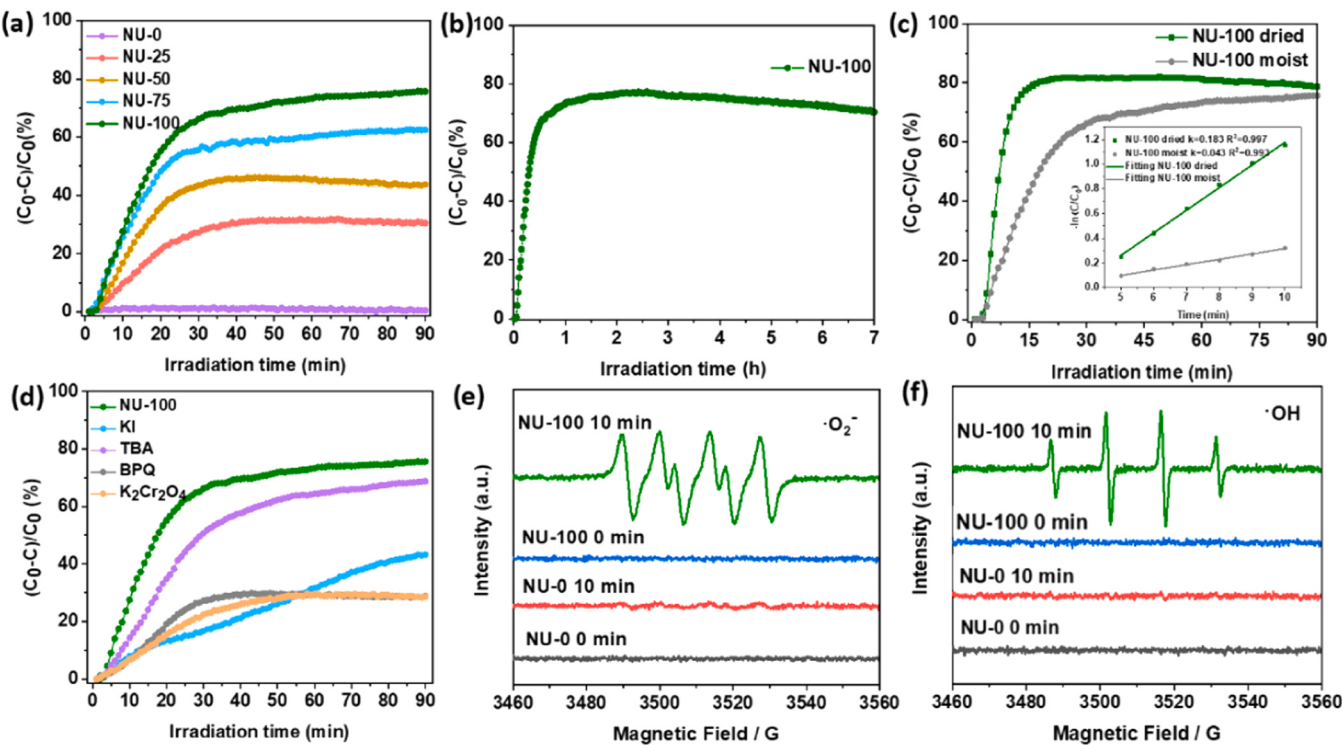


Fig. 5. (a) Photocatalytic NO removal performance over NU samples under moist atmosphere. (b) The durability test for photocatalytic NO oxidation over NU-100. (c) Photocatalytic NO removal performance over NU-100 in moist and dried atmosphere. (Inset c) Corresponding kinetic rate curves. (d) The photocatalytic performance of NO oxidation over NU-100 by using various trapping agents to capture active species in moist condition. Electron spin-trapping spectra signals of (e) DMPO-•O₂⁻ and (f) DMPO-•OH.

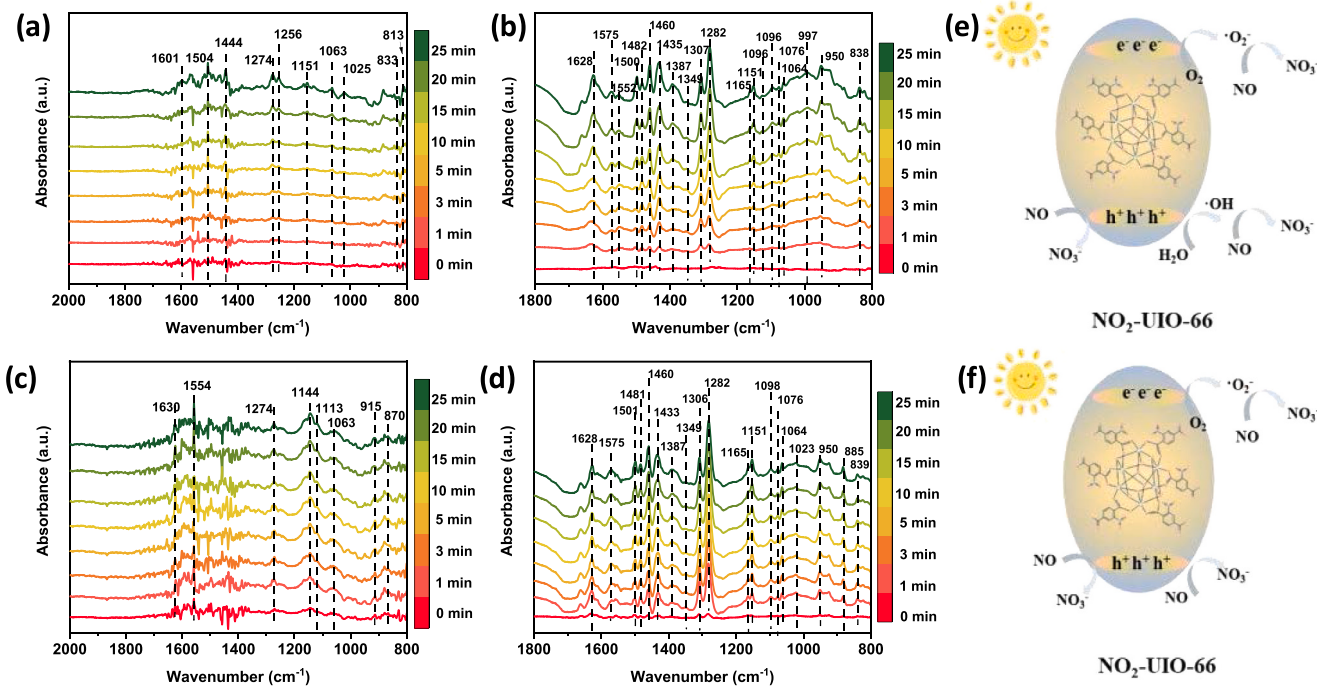


Fig. 6. *In situ* DRIFTS spectra of (a) NO adsorption in the dark and (b) NO oxidation reaction process under visible light irradiation at moist condition. (c) NO adsorption in the dark and (d) NO oxidation reaction process under visible light irradiation at dried condition. Schematic illustration of the mechanism of photocatalytic NO oxidation at (e) moist and (f) dried conditions, respectively.

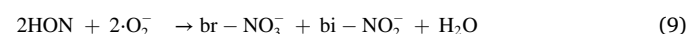
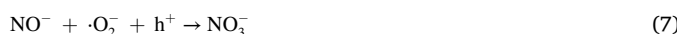
gas on the surface of NU-100. The intensity of the two peaks increased with the continuous adsorption process, implying the enrichment of NO gas on NU-100. Besides, the peaks corresponding to chelate nitrates

(813 cm⁻¹)^[48], NO₂ (833/1151 cm⁻¹)^[49], bidentate nitrates(1025 [49]/1445 cm⁻¹)^[50], monodentate nitrates (1256/1505 cm⁻¹)^[51], bridged nitrate (1602 cm⁻¹)^[52] developed gradually. The formation of

nitrites and nitrates during dark adsorption process are mainly attributed to the oxidation of NO gas by the strong oxidizing species in catalysts, such as a small amount of hydroxyl at the metal oxygen cluster in the organic framework of metals [53].

Under wet condition, a large amount of water molecules are absorbed to cover the active sites on the catalysts. So less active sites were exposed to NO molecules, which may lead to inadequate NO adsorption on the surface of catalysts. In contrast, most active sites are exposed for enhanced NO adsorption under dry condition. This analysis is further confirmed by the *in situ* DRIFTS results. As shown in Figs. 6a and 6c, the peaks of NO are appeared at 1063 cm⁻¹, and the peaks at 1274 cm⁻¹ are attributed to N₂O₂. With the continuous dark adsorption, the infrared absorption peaks at 1063 cm⁻¹ were enhanced, indicating that NO was continuously enriched on the NU-100 catalyst. The peaks at 915 cm⁻¹ were also gradually enhanced. This can be ascribed to the N₂O₄ species due to the increased concentration of NO adsorbed on the catalyst (O₂+2NO→2NO₂; 2NO₂→N₂O₄)[43]. For further understanding, the normalization of the two species (a) NO (1063 cm⁻¹), (b) N₂O₄ (915 cm⁻¹) over NU-100 during NO adsorption under moist and dried conditions are as shown in Fig. S16. Obviously, the adsorption strength of NU-100 on NO under dry condition was higher than that under wet condition, indicating their better adsorption of NO, and resulting in a faster NO removal rate under dry conditions.

As the gas adsorption equilibrium was established, a visible light ($\lambda > 400$ nm) was applied to initiate the NO photocatalytic oxidation processes over NU-100. As shown in Fig. 6b, according to the strong absorption bonds of nitrates (838 cm⁻¹), bridging nitrates (997/1076 cm⁻¹), monodentate nitrate (1282[10]/1500 cm⁻¹)[54], bidentate (at 1307/1435/1460/1482/1552/1575 cm⁻¹) nitrates[10,55], the stretching vibration of monodentate nitrates (1387 cm⁻¹), monodentate nitrite (1064 cm⁻¹)[56], bidentate nitrite (1126/1575 cm⁻¹) and nitrite (1151 cm⁻¹), it can conclude that the final products of photocatalytic oxidation of NO are mainly nitrate and nitrite. In addition, the peaks at 1628 cm⁻¹, 950 cm⁻¹, 1349 cm⁻¹ can be assigned to N₂O₂, N₂O₃, N₂O₄, respectively[57,58]. As the reaction proceeds, the intensity of N₂O₂ increase, indicating that the dimer N₂O₂ generates and accumulates gradually. The increased peak at 950 cm⁻¹ is indexed to the N₂O₃ gaseous intermediate product. Meanwhile, the peak at 1349 cm⁻¹ dropped, indicating that N₂O₄ was gradually oxidized into the final product. Intermediates including NOH[58], ionic intermediate state NO⁻[55] and NO⁺[59] are also detected at 1096, 1165 and 2300–2200 cm⁻¹, respectively. Similar results of *in situ* DRIFTS spectra of NU-100 under dry condition are achieved as shown in Fig. 6c-d. Based on the above analysis, h⁺, ·O₂ and ·OH work as active species in the photocatalytic removal of NO under moist condition, during which h⁺ and ·O₂ are considered to be the major ones. They also play key role under dry condition. Together with the results of *in situ* DRIFTS, the possible mechanism of photocatalytic NO oxidation over NU-100 under visible light irradiation is proposed, as exhibited in Fig. 6e-f and Fig. S17.



Under visible light irradiation, photo generated e⁻ and h⁺ are produced by NU-100 (Eq.1). The electrons react with O₂ to produce ·O₂ (Eq.2), and the h⁺ can oxidize NO to produce NO⁺ (Eq.3). The produced NO⁺ will interact with e⁻ or ·O₂ to generate nitrate (Eqs.4 and 5). At the same time, e⁻ can also reduce NO to NO⁻ or intermediate HON (Eqs.6 and 8). NO⁻ is further oxidized to nitrate by h⁺ and ·O₂ (Eq.7), and HON is also oxidized to nitrate or nitrite by ·O₂ (Eq.9). In addition, holes can oxidize the water molecules present in the system to generate ·OH under moist condition (Eq.10), which further oxidize NO and the dimer N₂O₂ to N₂O₃ and N₂O₄ (Eqs.11 to 13). While under dried conditions, in the absence of hydroxyl radicals, holes and superoxide radicals can also achieve this process (Eqs.14 to 15). At last, the intermediate species are oxidized to nitrate by ·O₂ (Eq.16).

4. Conclusions

In summary, we developed a -NO₂ functionalized MOF photocatalyst by microwave-assisted solvothermal method. This NO₂-UiO-66(Zr) exhibited high activity and strong durability in visible light induced photocatalytic NO_x purification in gas-phase in both moist and dried conditions. The strong electron-withdrawing property of -NO₂ and the large specific surface areas of MOFs increase the material's ability to adsorb the electron-rich gas NO, resulting in the enrichment of NO on the surface of this photocatalyst. At the same time, -NO₂ is a chromophore which can form a conjugate with the electron cloud on the benzene ring to deepen the color of the material to affect the light absorption performance of the catalysts. With the increase of the amount of modified -NO₂ in the skeleton, the absorption of light was successfully extended from the ultraviolet to visible light. This work developed a new strategy to modify MOF based photocatalysts for regulated band structures and the promoted enrichment ability of NO. It may be potentially applied to the other electron withdrawing groups (such as cyano group, bromine atom, etc.) for efficient modification of MOFs based photocatalysts.

CRediT authorship contribution statement

Jingjing Zhao: Methodology, Investigation, Formal analysis, Data curation, Writing – original draft. **Shuangjun Li:** Methodology, Investigation, Formal analysis, Data curation. **Rui Liang:** Software, Methodology, Formal analysis, Data curation. **Qing Wang:** Software, Methodology, Formal analysis, Data curation. **Yi Li:** Data curation. **Xiaoyan Liu:** Writing – review & editing, Writing – original draft, Supervision, Investigation, Funding acquisition. **Dieqing Zhang:** Writing – review & editing, Writing – original draft, Supervision, Investigation, Funding acquisition, Conceptualization. **Hexing Li:** Writing – review & editing, Writing – original draft, Supervision, Resources, Funding acquisition, Conceptualization.

Declaration of Competing Interest

The authors declare that they have no known competing financial interests or personal relationships that could have appeared to influence the work reported in this paper.

Data Availability

Data will be made available on request.

Acknowledgments

This work was supported by the National Natural Science Foundation of China (22236005, 22376142, 22305157, 22176127, 22022608), National Key Research and Development Program of China (2020YFA0211004), the Shanghai Engineering Research Center of Green Energy Chemical Engineering (18DZ2254200), and “111” Innovation and Talent Recruitment Base on Photochemical and Energy Materials (D18020), the Shanghai Government (22010503400, 218014346, 18SG41, YDZX20213100003002, 23520711100), Shanghai Scientific and Technological Innovation Project (21DZ1206300).

Appendix A. Supporting information

Supplementary data associated with this article can be found in the online version at [doi:10.1016/j.apcatb.2024.123982](https://doi.org/10.1016/j.apcatb.2024.123982).

References

- [1] P.M. Edwards, S.S. Brown, J.M. Roberts, R. Ahmadov, R.M. Banta, J.A. deGouw, W. P. Dube, R.A. Field, J.H. Flynn, J.B. Gilman, M. Graus, D. Helming, A. Koss, A. O. Langford, B.L. Lefer, B.M. Lerner, R. Li, S.M. Li, S.A. McKeen, S.M. Murphy, D. D. Parrish, C.J. Senff, J. Soltis, J. Stutz, C. Sweeney, C.R. Thompson, M.K. Trainer, C. Tsai, P.R. Veres, R.A. Washenfelder, C. Warneke, R.J. Wild, C.J. Young, B. Yuan, R. Zamora, High winter ozone pollution from carbonyl photolysis in an oil and gas basin, *Nature* 514 (2014) 351–354.
- [2] S.C. Anenberg, J. Miller, R. Minjares, L. Du, D.K. Henze, F. Lacey, C.S. Malley, L. Emberson, V. Franco, Z. Klimont, C. Heyes, Impacts and mitigation of excess diesel-related NO_x emissions in 11 major vehicle markets, *Nature* 545 (2017) 467–471.
- [3] K. Skalska, J.S. Miller, S. Ledakowicz, Trends in NO_x abatement: a review, *Sci. Total Environ.* 408 (2010) 3976–3989.
- [4] D. Damma, P. Ettireddy, B. Reddy, P. Smirniotis, A review of low temperature NH₃-SCR for removal of NO_x, *Catalysts* 9 (2019) 349.
- [5] L. Schill, R. Fehrmann, Strategies of coping with deactivation of NH₃-SCR catalysts due to biomass firing, *Catalysts* 8 (2018) 135.
- [6] H. Chen, D. Chen, S. Fan, L. Hong, D. Wang, SNCR De-NO_x within a moderate temperature range using urea-spiked hydrazine hydrate as reductant, *Chemosphere* 161 (2016) 208–218.
- [7] Liu, Yu, Ma, Dan, Luo, Dai, A critical review of recent progress and perspective in practical denitrification application, *Catalysts* 9 (2019) 771.
- [8] J. Shao, Y. Tao, K.K. Hansen, Highly selective NO_x reduction for diesel engine exhaust via an electrochemical system, *Electrochim. Commun.* 72 (2016) 36–40.
- [9] Y. Boyjoo, H. Sun, J. Liu, V.K. Pareek, S. Wang, A review on photocatalysis for air treatment: From catalyst development to reactor design, *Chem. Eng. J.* 310 (2017) 537–559.
- [10] H. Shang, M. Li, H. Li, S. Huang, C. Mao, Z. Ai, L. Zhang, Oxygen vacancies promoted the selective photocatalytic removal of no with blue TiO₂ via simultaneous molecular oxygen activation and photogenerated hole annihilation, *Environ. Sci. Technol.* 53 (2019) 6444–6453.
- [11] K. Fujiwara, U. Müller, S.E. Pratsinis, Pd subnano-clusters on TiO₂ for solar-light removal of NO, *ACS Catal.* 6 (2016) 1887–1893.
- [12] S. Xiao, Z. Wan, J. Zhou, H. Li, H. Zhang, C. Su, W. Chen, G. Li, D. Zhang, H. Li, Gas-phase photoelectrocatalysis for breaking down nitric oxide, *Environ. Sci. Technol.* 53 (2019) 7145–7154.
- [13] X. Chen, H. Zhang, D. Zhang, Y. Miao, G. Li, Controllable synthesis of mesoporous multi-shelled ZnO microspheres as efficient photocatalysts for NO oxidation, *Appl. Surf. Sci.* 435 (2018) 468–475.
- [14] L. Fan, K. Wang, K. Xu, Z. Liang, H. Wang, S.F. Zhou, G. Zhan, Structural isomerism of two Ce-BTC for fabricating Pt/CeO₂ nanorods toward low-temperature CO oxidation, *Small* 16 (2020) e2003597.
- [15] L. Feng, J. Pang, P. She, J.L. Li, J.S. Qin, D.Y. Du, H.C. Zhou, Metal-organic frameworks based on Group 3 and 4 metals, *Adv. Mater.* 32 (2020) e2004414.
- [16] M. Taheri, T. Tsuzuki, Photo-accelerated hydrolysis of metal organic framework ZIF-8, *ACS Mater. Lett.* 3 (2021) 255–260.
- [17] X. Mu, J. Jiang, F. Chao, Y. Lou, J. Chen, Ligand modification of UiO-66 with an unusual visible light photocatalytic behavior for RhB degradation, *Dalton Trans.* 47 (2018) 1895–1902.
- [18] N.S. Abdul Mubarak, K.Y. Foo, R. Schneider, R.M. Abdelhameed, S. Sabar, The chemistry of MIL-125 based materials: structure, synthesis, modification strategies and photocatalytic applications, *J. Environ. Chem. Eng.* 10 (2022) 106883.
- [19] G. Capano, F. Ambrosio, S. Kampouri, K.C. Stylianou, A. Pasquarello, B. Smit, On the electronic and optical properties of metal-organic frameworks: case study of MIL-125 and MIL-125-NH₂, *J. Phys. Chem. C.* 124 (2020) 4065–4072.
- [20] H. Liu, T. Liu, T. Huang, Z. Fang, L. Li, Q. Yin, R. Cao, X. Gong, T. Liu, Trace of molecular doping in metal-organic frameworks: drastic change in the electronic band structure with a preserved topology and porosity, *J. Mater. Chem. A* 8 (2020) 12370–12377.
- [21] X. Chen, Y. Cai, R. Liang, Y. Tao, W. Wang, J. Zhao, X. Chen, H. Li, D. Zhang, NH₂-UiO-66(Zr) with fast electron transfer routes for breaking down nitric oxide via photocatalysis, *Appl. Catal. B Environ.* 267 (2020) 118687.
- [22] X. Chen, S. Xiao, H. Wang, W. Wang, Y. Cai, G. Li, M. Qiao, J. Zhu, H. Li, D. Zhang, Y. Lu, MOFs conferred with transient metal centers for enhanced photocatalytic activity, *Angew. Chem. Int. Ed.* 59 (2020) 17182–17186.
- [23] S.Y. Han, D.L. Pan, H. Chen, X.B. Bu, Y.X. Gao, H. Gao, Y. Tian, G.S. Li, G. Wang, S. L. Cao, C.Q. Wan, G.C. Guo, A methylthio-functionalized-MOF photocatalyst with high performance for visible-light-driven H₂ evolution, *Angew. Chem. Int. Ed.* 57 (2018) 9864–9869.
- [24] L. Shen, R. Liang, M. Luo, F. Jing, L. Wu, Electronic effects of ligand substitution on metal-organic framework photocatalysts: the case study of UiO-66, *Phys. Chem. Chem. Phys.* 17 (2015) 117–121.
- [25] M. Kalaj, J.M. Palomba, K.C. Bentz, S.M. Cohen, Multiple functional groups in UiO-66 improve chemical warfare agent simulant degradation, *Chem. Commun.* 55 (2019) 5367–5370.
- [26] Z.H. Rada, H.R. Abid, H. Sun, J. Shang, J. Li, Y. He, S. Liu, S. Wang, Effects of -NO₂ and -NH₂ functional groups in mixed-linker Zr-based MOFs on gas adsorption of CO₂ and CH₄, *Prog. Nat. Sci.: Mater. Int.* 28 (2018) 160–167.
- [27] S.S. Nagarkar, A.V. Desai, S.K. Ghosh, A nitro-functionalized metal-organic framework as a reaction-based fluorescence turn-on probe for rapid and selective H₂S detection, *Chemistry* 21 (2015) 9994–9997.
- [28] M. Kandiah, M.H. Nilsen, S. Usseglio, S. Jakobsen, U. Olsbye, M. Tilset, C. Larabi, E.A. Quadrelli, F. Bonino, K.P. Lillerud, Synthesis and stability of tagged UiO-66 Zr-MOFs, *Chem. Mater.* 22 (2010) 6632–6640.
- [29] J.H. Cavka, S. Jakobsen, U. Olsbye, N. Guillou, C. Lamberti, S. Bordiga, K. P. Lillerud, A new zirconium inorganic building brick forming metal organic frameworks with exceptional stability, *J. Am. Chem. Soc.* 130 (2008) 13850–13851.
- [30] W. Yang, J. Wang, Y. Han, X. Luo, W. Tang, T. Yue, Z. Li, Robust MOF film of self-rearranged UiO-66-NO₂ anchored on gelatin hydrogel via simple thermal-treatment for efficient Pb(II) removal in water and apple juice, *Food Control* 130 (2021) 108409.
- [31] L. Shen, R. Liang, M. Luo, F. Jing, L. Wu, Electronic effects of ligand substitution on metal-organic framework photocatalysts: the case study of UiO-66, *Phys. Chem. Chem. Phys.* 17 (2015) 117–121.
- [32] V. Colombo, C. Montoro, A. Maspero, G. Palmisano, N. Masciocchi, S. Galli, E. Barea, J.A.R. Navarro, Tuning the adsorption properties of isoreticular pyrazolate-based metal-organic frameworks through ligand modification, *J. Am. Chem. Soc.* 134 (2012) 12830–12843.
- [33] T.D. Duong, S.A. Sapchenko, I. da Silva, H.G.W. Godfrey, Y. Cheng, L.L. Daemen, P. Manuel, A.J. Ramirez-Cuesta, S. Yang, M. Schröder, Optimal binding of acetylene to a nitro-decorated metal-organic framework, *J. Am. Chem. Soc.* 140 (2018) 16006–16009.
- [34] W. Zhu, X. Chen, C. Li, Z. Liu, C. Liang, Manipulating morphology and surface engineering of spinel cobalt oxides to attain high catalytic performance for propane oxidation, *J. Catal.* 396 (2021) 179–191.
- [35] S. Mo, Q. Zhang, Y. Sun, M. Zhang, J. Li, Q. Ren, M. Fu, J. Wu, L. Chen, D. Ye, Gaseous CO and toluene co-oxidation over monolithic core-shell Co₃O₄-based hetero-structured catalysts, *J. Mater. Chem. A* 7 (2019) 16197–16210.
- [36] T. Cai, J. Yuan, L. Zhang, L. Yang, Q. Tong, M. Ge, B. Xiao, X. Zhang, K. Zhao, D. He, Ni-Co-O solid solution dispersed nanocrystalline Co₃O₄ as a highly active catalyst for low-temperature propane combustion, *Catal. Sci. Technol.* 8 (2018) 5416–5427.
- [37] Y. Meng, W. Song, H. Huang, Z. Ren, S.Y. Chen, S.L. Suib, Structure-property relationship of bifunctional MnO₂ nanostructures: highly efficient, ultra-stable electrochemical water oxidation and oxygen reduction reaction catalysts identified in alkaline media, *J. Am. Chem. Soc.* 136 (2014) 11452–11464.
- [38] Q. Li, J. Zhao, H. Shang, Z. Ma, H. Cao, Y. Zhou, G. Li, D. Zhang, H. Li, Singlet oxygen and mobile hydroxyl radicals co-operating on gas-solid catalytic reaction interfaces for deeply oxidizing NO_x, *Environ. Sci. Technol.* 56 (2022) 5830–5839.
- [39] M.C. Chen, D.G. Chen, P.T. Chou, Fluorescent chromophores containing the nitro group: relatively unexplored emissive properties, *ChemPlusChem* 86 (2021) 11–27.
- [40] K. Hendrickx, D. Vanpoucke, K. Leus, K. Lejaeghere, A. Van Yperen-De Deyne, V. Van Speybroeck, P. Van Der Voort, K. Hemelsoet, Understanding intrinsic light absorption properties of UiO-66 frameworks: a combined theoretical and experimental study, *Inorg. Chem.* 54 (2015) 10701–10710.
- [41] S. Xiao, D. Pan, R. Liang, W. Dai, Q. Zhang, G. Zhang, C. Su, H. Li, W. Chen, Bimetal MOF derived mesocrystal ZnCo₂O₄ on rGO with high performance in visible-light photocatalytic NO oxidization, *Appl. Catal. B Environ.* 236 (2018) 304–313.

[42] S. Wang, W. Cui, B. Lei, X. Dong, Y. Tang, F. Dong, Targeted NO oxidation and synchronous NO₂ inhibition via Oriented ¹O₂ formation based on lewis acid site adjustment, Environ. Sci. Technol. 57 (2023) 12890–12900.

[43] S. Li, H. Shang, Y. Tao, P. Li, H. Pan, Q. Wang, S. Zhang, H. Jia, H. Zhang, J. Cao, B. Zhang, R. Zhang, G. Li, Y. Zhang, D. Zhang, H. Li, Hydroxyl radical-mediated efficient photoelectrocatalytic NO oxidation with simultaneous nitrate storage using a flow photoanode reactor, Angew. Chem. Int. Ed. 62 (2023) e202305538.

[44] X. Huang, X. Shu, J. Li, Z. Cui, S. Cao, W. Chen, J. Yin, G. Yan, H. Zhao, J. Hu, Z. Yang, Y. Wang, DFT study on type-II photocatalyst for overall water splitting: g-GaN/C₂N van der Waals heterostructure, Int. J. Hydron. Energy 48 (2023) 12364–12373.

[45] S. Hussain, L. Hou, Q. Li, First-principles investigations of novel BaSb_{2(1-x)}Bi_{2x}O₆ solid solutions applying for water splitting, Appl. Surf. Sci. 612 (2023) 155832.

[46] Z. Wang, Y. Huang, M. Chen, X. Shi, Y. Zhang, J. Cao, W. Ho, S.C. Lee, Roles of N-Vacancies over porous g-C₃N₄ microtubes during photocatalytic NO_x removal, ACS Appl. Mater. Interfaces 11 (2019) 10651–10662.

[47] S. Xiao, D. Zhang, D. Pan, W. Zhu, P. Liu, Y. Cai, G. Li, H. Li, A chloroplast structured photocatalyst enabled by microwave synthesis, Nat. Commun. 10 (2019) 1570.

[48] F. Rao, G. Zhu, M. Hojamberdiev, W. Zhang, S. Li, J. Gao, F. Zhang, Y. Huang, Y. Huang, Uniform Zn²⁺-doped BiOI microspheres assembled by ultrathin nanosheets with tunable oxygen vacancies for super-stable removal of NO, J. Phys. Chem. C. 123 (2019) 16268–16280.

[49] Z. Zhao, Y. Cao, F. Dong, F. Wu, B. Li, Q. Zhang, Y. Zhou, The activation of oxygen through oxygen vacancies in BiOCl/PPy to inhibit toxic intermediates and enhance the activity of photocatalytic nitric oxide removal, Nanoscale 11 (2019) 6360–6367.

[50] H. Wang, W. Zhang, X. Li, J. Li, W. Cen, Q. Li, F. Dong, Highly enhanced visible light photocatalysis and in situ FT-IR studies on Bi metal@defective BiOCl hierarchical microspheres, Appl. Catal. B Environ. 225 (2018) 218–227.

[51] M. Kantcheva, Identification, stability, and reactivity of NO_x species adsorbed on titania-supported manganese catalysts, J. Catal. 204 (2001) 479–494.

[52] N. Tang, Y. Liu, H. Wang, Z. Wu, Mechanism study of NO catalytic oxidation over MnO_x/TiO₂ catalysts, J. Phys. Chem. C. 115 (2011) 8214–8220.

[53] Q. Yang, S. Li, R. Liang, L. Gao, S. Zhang, J. Jia, Y. Liu, R. Lyv, G. Li, S. Xiao, D. Zhang, Microwave assisted synthesis of PQ-GDY@NH₂-UIO-66(Zr) for improved photocatalytic removal of NO under visible light, J. Environ. Sci. 134 (2023) 126–137.

[54] L. Sivachandiran, F. Thevenet, A. Rousseau, D. Bianchi, NO₂ adsorption mechanism on TiO₂: An in-situ transmission infrared spectroscopy study, Appl. Catal. B Environ. 198 (2016) 411–419.

[55] W. Huo, W. Xu, T. Cao, X. Liu, Y. Zhang, F. Dong, Carbonate-intercalated defective bismuth tungstate for efficiently photocatalytic NO removal and promotion mechanism study, Appl. Catal. B Environ. 254 (2019) 206–213.

[56] M. Chen, Z. Wang, D. Han, F. Gu, G. Guo, Porous ZnO polygonal nanoflakes: synthesis, use in high-sensitivity NO₂ gas sensor, and proposed mechanism of gas sensing, J. Phys. Chem. C. 115 (2011) 12763–12773.

[57] H. Wang, Y. Sun, G. Jiang, Y. Zhang, H. Huang, Z. Wu, S.C. Lee, F. Dong, Unraveling the mechanisms of visible light photocatalytic NO purification on earth-abundant insulator-based core-shell heterojunctions, Environ. Sci. Technol. 52 (2018) 1479–1487.

[58] X. Li, W. Zhang, J. Li, G. Jiang, Y. Zhou, S. Lee, F. Dong, Transformation pathway and toxic intermediates inhibition of photocatalytic NO removal on designed Bi metal@defective Bi₂O₂SiO₃, Appl. Catal. B Environ. 241 (2019) 187–195.

[59] P. Chen, H. Wang, H. Liu, Z. Ni, J. Li, Y. Zhou, F. Dong, Directional electron delivery and enhanced reactants activation enable efficient photocatalytic air purification on amorphous carbon nitride co-functionalized with O/La, Appl. Catal. B Environ. 242 (2019) 19–30.